

# Unveiling the Optoelectronic Potential of Vacancy-Ordered Double Perovskites: A Computational Deep Dive

Surajit Adhikari\*, Ayan Chakravorty, and Priya Johari\*

*Department of Physics, School of Natural Sciences,  
Shiv Nadar Institution of Eminence, Greater Noida,  
Gautam Buddha Nagar, Uttar Pradesh 201314, India*

Lead-free perovskite materials have emerged as key players in optoelectronics, showcasing exceptional optical and electronic properties, alongside being environmentally friendly and non-toxic elements. Recently, among studied perovskite materials, vacancy-ordered double perovskites (VODPs) stand out as a promising alternative. In this study, we captured the electronic, optical, excitonic, and polaronic properties of a series of VODPs with the chemical formula  $\text{Rb}_2\text{BX}_6$  ( $\text{B} = \text{Si, Ge, Sn, Pt}$ ;  $\text{X} = \text{Cl, Br, I}$ ) using first-principles calculations. Our results indicate these materials exhibit high stability and notable electronic and optical properties. The calculated  $G_0W_0$  bandgap values of these perovskites fall within the range of 0.56 to 6.12 eV. Optical properties indicate strong infrared to ultraviolet light absorption across most of the systems. Additionally, an analysis of excitonic properties reveals low to moderate exciton-binding energies and variable exciton lifetimes, implying higher quantum yield and conversion efficiency. Furthermore, utilizing the Feynman polaron model, polaronic parameters are evaluated, and for the majority of systems, charge-separated polaronic states are less stable than bound excitons. Finally, an investigation of Polaronic mobility reveals high polaron mobility for electrons ( $3.33\text{--}85.11 \text{ cm}^2\text{V}^{-1}\text{s}^{-1}$ ) compared to previously reported Cs-based VODP materials. Overall, these findings highlight Rb-based VODPs as promising candidates for future optoelectronic applications.

## I. INTRODUCTION:

The development of halide perovskites (HPs) for optoelectronic applications has made tremendous progress in recent years. Primitively, organic-inorganic lead-halide perovskites  $\text{APbX}_3$  ( $\text{A} = \text{Rb, Cs, CH}_3\text{NH}_3$ ;  $\text{X} = \text{Cl, Br, and I}$ ) drew a lot of attention due to their strong optical absorption, variable energy gap, long carrier diffusion length, and excellent power conversion efficiencies[1]. Due to their exceptional optoelectronic properties, organic-inorganic lead halide perovskites are highly sought after for a range of applications, including efficient solar cells, information storage, humidity sensors, LEDs, lasers, and photoelectric detectors. The power conversion efficiency (PCE) of these perovskite solar cells has reached up to 24.2%[2], surpassing some silicon-based thin-film solar cells. Consequently, organic-inorganic lead halide perovskites have emerged as the most extensively researched and cost-effective materials for photovoltaic energy conversion in recent years.

Despite their outstanding performance, the practical applications of  $\text{CH}_3\text{NH}_3$ -based materials are limited due to the volatility and moisture sensitivity of  $\text{CH}_3\text{NH}_3$ , as well as the toxic nature of lead (Pb), and their poor long-term stability. This highlights the need to explore Pb-free hybrid halide perovskites.[3]. To get rid of lead, a new approach has been developed where two  $\text{Pb}^{2+}$  cations are replaced by a combination of one monovalent cation ( $\text{M}^+$ ) and one trivalent cation ( $\text{M}^{3+}$ ). This substitution gives rise to a new class of perovskites, called double perovskites with the formula  $\text{A}_2\text{M(I)M(III)X}_6$ , where A represents a monovalent cation, and X represents halides such as Cl, Br, or I. Several Pb-free double halide perovskites have been explored in past few years, such as  $\text{Cs}_2\text{MSbX}_6$  ( $\text{M} = \text{Cu, Ag, Na, K, Rb, Cs, and X} = \text{Cl, Br}$ )[4] and  $\text{Cs}_2\text{YCuX}_6$  ( $\text{X} = \text{Cl, Br, I}$ )[5]. These lead-free halide double perovskite materials have shown to exhibit outstanding optoelectronic properties such as high optical absorption, tunable bandgap, broad absorption spectrum, small carrier effective masses, long charge diffusion lengths and high charge carrier mobility[6, 7].

While these lead-free alternatives show promise, they still require significant efficiency improvements to match the performance of lead-halide perovskites. One major challenge of lead-free halide double perovskites is their typically large and indirect bandgaps, which hinder their efficiency in comparison to lead-halide perovskites. This limitation restricts their potential for applications like high-efficiency solar cells and optoelectronic devices. To address these limitations, vacancy-ordered double perovskites (VODPs), a class of double perovskites, with the formula  $\text{A}_2\text{BX}_6$  have emerged as a more efficient alternative. These complexes are eco-friendly, containing interesting luminescent, optical, dielectric, and magnetic properties and have applications in modern semiconductor devices[8]. The VODP materials can be viewed as a derivative structure of the traditional  $\text{ABX}_3$  by orderly deleting half of the B atoms in the core of

---

\* sa731@snu.edu.in, priya.johari@snu.edu.in

the octahedron in a regular motif[9]. VODPs, with B in a '+4' oxidation state, demonstrate enhanced stability in the presence of air and moisture compared to traditional  $ABX_3$  perovskites[8, 10]. This structural modification expands the composition space, allowing them for chemical tuning and property optimization. The transition from traditional single and double halide perovskites [ $ABX_3$  and  $A_2M(I)M(III)X_6$ ] to  $A_2BX_6$ , thus presents exciting prospects for advancing optoelectronic materials with broader applications. In contrast, there is relatively little room for chemical modification in the halide  $ABX_3$  structure, and only a few halide perovskites can form; those have already been thoroughly studied[11].

Recent research based on the  $A_2BX_6$  has opened new possibilities for a stabilized and eco-friendly solar cell material[12]. Compounds such as  $Rb_2PdI_6$ ,  $Rb_2PdBr_6$ , and  $Cs_2PtI_6$  exhibit ideal bandgaps, high dielectric constants, and strong absorption coefficients, making them promising for solar cell applications due to their robust nature and environmental benefits[13]. Zhao et al. used DFT-based first-principles calculations to examine the electronic and optical properties of inorganic  $A_2PtI_6$  ( $A = Rb$  or  $Cs$ ) compounds[14], which having bandgaps of 1.15 eV and 1.29 eV, suitable for solar cells and optoelectronic devices. Jiang et al. determined the direct bandgaps and computed the mechanical, thermal, electrical, and optical properties of  $Cs_2SnX_6$  ( $X = Cl, Br, \text{ and } I$ )[15]. Several materials, including  $Cs_2TeI_6$ ,  $Cs_2SnI_6$ , and  $Cs_2TiI_6$ , with suitable bandgaps are known in theory and experiment[9, 16, 17]. In the context of DFT and hybrid functional (HSE06), the stability and electronic structure of  $A_2BX_6$  ( $A = K, Rb, Cs$ ;  $B = Si, Ge, Sn, Pb, Ni, Pd, Pt, Se, Te$ ; and  $X = Cl, Br, I$ ) have been studied [18].

The synthesis of thin films and single crystals of  $Cs_2TeI_6$  has been done having an optical bandgap of 1.5 eV and  $Cs_2PdBr_6$  showing a bandgap of 1.69 eV and strong long-term stability[19, 20]. Additionally, microcrystals of  $Rb_2HfCl_6$  and various  $Rb_2TeX_6$  ( $X=Cl, Br, I$ ) compounds have been experimentally synthesized[8, 21]. Recent advancements include the synthesis of  $Rb_2SnCl_6$ ,  $Rb_2SnBr_6$ ,  $K_2SnBr_6$ , and  $Rb_2SnI_6$ [22]. Recently, the potential for using  $Cs_2SnI_6$  in solar technology has also been investigated[9]. The optoelectronic properties of various VODPs are significantly influenced by the B-site cation, with the choice of element affecting their structural and tunable optoelectronic characteristics due to the  $[BX_6]^-$  octahedra. However,  $Sn^{2+}$  and  $Ge^{2+}$  cations are prone to oxidation into  $Sn^{4+}$  and  $Ge^{4+}$ , which can lead to instability in perovskite solar cells (PSCs) based on these materials. Despite this challenge,  $Cs_2SnI_6$ , with its unique VODP structure, shows potential as a light-absorbing layer for PSCs[23]. This underscores the necessity of exploring Sn- and Ge-based VODPs further to overcome stability issues and optimize their performance in optoelectronic applications.. Another fact is that crystalline Si solar cells are widely used in industry but are more expensive to produce, which has prompted researchers to investigate the theoretical features of Si-based DPs.  $Cs_2SiI_6$  has already been studied computationally and it possesses a direct bandgap of 2.72 eV. Till now, according to our report,  $Rb_2SiBr_6$  and  $Rb_2GeBr_6$  have yet to be studied experimentally and theoretically.

In this contribution, we employed first-principles density functional theory (DFT) and many-body perturbation theory (MBPT) based simulations to extensively explore the phase stability and optoelectronic properties of lead (Pb)-free  $Rb_2BX_6$  ( $B = Si, Ge, Sn, Pt$ ;  $X = Cl, Br, I$ ) VODPs. All compounds maintain a stable, standard cubic double perovskite structure with alternating B-site vacancies, showing promising mechanical stability and flexibility. Electronic properties reveal that these materials have a direct bandgap except  $Rb_2PtBr_6$  and  $Rb_2PtI_6$ . Then, utilizing excited-state methods, we computed the optical characteristics using the GW-BSE methodology based on the many-body perturbation theory (MBPT). The Bethe-Salpeter equation (BSE)[24, 25], on top of a single-shot  $GW(G_0W_0)$ @PBE[26], has been solved to ascertain the electronic contribution to the dielectric function. Further, the ionic contribution to the dielectric function is obtained using density functional perturbation theory (DFPT). Additionally, our results indicate low carrier effective mass, high mobility, varied exciton lifetimes, and low to moderate exciton binding energies. Finally, we determined several polaronic properties, suggesting that most of the materials have high polaron mobility facilitating efficient charge transport in optoelectronic devices. Overall, this study offers a thorough analysis of a number of  $Rb_2BX_6$  compounds and creates a pathway for the intriguing lead-free perovskite possibilities, which have significant promise for next-generation optoelectronic and photovoltaic devices.

## II. COMPUTATIONAL DETAILS :

In our present study, first-principles density-functional theory (DFT) and many-body perturbation theory (MBPT) based computations were carried out using the Vienna ab initio simulation package (VASP)[27, 28]. The projected augmented wave (PAW) approach was employed in all calculations to accurately model the interactions between the valence electrons and the atomic core[29]. The PAW pseudopotentials with valence shell electrons of each atom were being considered as follows: 9 for Rb -  $4s^24p^65s^1$ , 4 for Si -  $3s^23p^2$ , 14 for Ge -  $3d^{10}4s^24p^2$ , 14 for Sn -  $4d^{10}5s^25p^2$ , 10 for Pt -  $5d^96s^1$ , 7 for Cl -  $3s^23p^5$ , 7 for Br -  $4s^24p^5$ , and 7 for I -  $5s^25p^5$ . The exchange-correlation (xc) functional of Perdew, Burke, and Ernzerhof (PBE), which is based on the generalized gradient approximation (GGA), was used to account for the electron-electron interactions[30]. Utilizing the conjugate gradient approach, the total energy was minimized to generate the optimal structural parameters for each of the VODP system. The calculations for all the systems were

performed using an optimized plane-wave cutoff energy of 400 eV. The convergence conditions for self-consistent-field iteration and geometry relaxation in all calculations were set at  $10^{-6}$  eV for energy and 0.01 eV/Å for Hellmann-Feynman forces on each atom. PBE xc functional with  $\Gamma$ -centered  $\mathbf{k}$ -point of  $4 \times 4 \times 4$  grid was used for structural optimization. The PBE functional, however, are known to underestimate energy bandgaps and optical characteristics due to the self-interaction error. To obtain more accurate electronic structures, hybrid Heyd–Scuseria–Ernzerhof (HSE06)[25] and many-body perturbation theory (MBPT) based  $G_0W_0@PBE$ [31, 32] calculations were performed for all the systems. Note that the band structures were calculated using the PBE xc functionals, taking into account the spin-orbit coupling effect. In addition, the density of state (DOS) computations were performed using the hybrid HSE06 functional with  $\Gamma$ -centered  $6 \times 6 \times 6$   $\mathbf{k}$ -point grid. To ascertain accurate optical properties, we solved the MBPT-based Bethe-Salpeter equation (BSE)[33, 34] on top of single-shot  $GW(G_0W_0)@PBE$ [31, 32] computations. In the GW-BSE calculations, we utilized  $\Gamma$ -centered  $4 \times 4 \times 4$   $\mathbf{k}$ -grid, achieving complete convergence with an impressive number of NBANDS, specifically 540. The electron-hole kernel for BSE calculations was constructed using 6 occupied and 6 unoccupied states. For each system, the ionic contribution to the dielectric function was computed using density functional perturbation theory (DFPT)[35] with a  $4 \times 4 \times 4$   $\mathbf{k}$ -point grid.

### III. RESULTS AND DISCUSSIONS:

In this study, we performed a thorough and systematic investigation of vacancy-ordered double perovskites  $Rb_2BX_6$  (B = Si, Ge, Sn, Pt; X = Cl, Br, I) to evaluate their potential optoelectronic properties. The following sections delve into a detailed analysis of the stability, along with the structural, electronic, optical, excitonic, and polaronic properties of these  $Rb_2BX_6$  compounds, offering fundamental insights to inform and guide future experimental research.

#### A. Structural Properties:

##### 1. Crystal Structure:

The  $Rb_2BX_6$  double perovskites, having elements Rb, Si, Ge, Sn, Pt, Cl, Br, and I, showcase an orderly face-centered cubic crystal structure designated by the space group  $Fm\bar{3}m$  (225). This configuration is similar to insufficient B-site  $ABX_3$  perovskite materials that have discrete  $[BX_6]$  clusters. In this configuration, 12 halogen ions surround the A-site cations (Rb), while 6 halogen ions coordinate with the B-site atoms.

In the crystal structure, Rb atoms find their place at specific 8c Wyckoff positions with coordinates (0.25, 0.25, 0.25). Meanwhile, B atoms occupy 4a Wyckoff positions at (0, 0, 0), while X atoms are located at 24e Wyckoff positions with coordinates (x, 0, 0), where x hovers around 0.20. In this arrangement, Rb atoms reside between  $[BX_6]$  octahedra, surrounded by 12 halogen atoms, while B atoms take position at the corners and face-centered spots of  $[BX_6]$  octahedra.

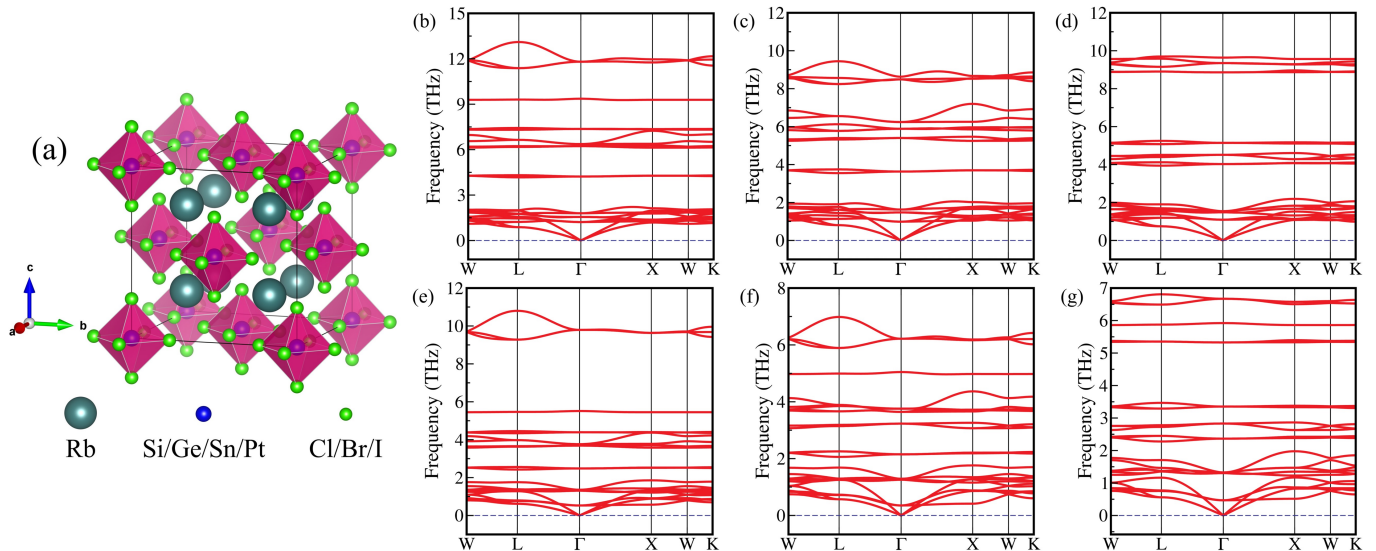


Figure 1. (a) Crystal structure of  $\text{Rb}_2\text{BX}_6$  ( $\text{B} = \text{Si}, \text{Ge}, \text{Sn}, \text{Pt}$ ;  $\text{X} = \text{Cl}, \text{Br}, \text{I}$ ) VODPs, and phonon dispersion curves of (b)  $\text{Rb}_2\text{SiCl}_6$ , (c)  $\text{Rb}_2\text{GeCl}_6$ , (d)  $\text{Rb}_2\text{PtCl}_6$ , (e)  $\text{Rb}_2\text{SiBr}_6$ , (f)  $\text{Rb}_2\text{GeBr}_6$ , and (g)  $\text{Rb}_2\text{PtBr}_6$  VODP, respectively, calculated with the DFPT method.

Table I provides an overview of the optimized lattice parameters of the analyzed VODPs. We find that our computed lattice parameters match well with the earlier theoretical and experimental data [13, 36–39]. Based on our calculations, we observe a consistent pattern of the lattice constant increasing gradually when transitioning from lower to higher atomic radius of the halogen atoms. We also notice a comparable trend in bond lengths, where the distances for both Rb-X and B-X bonds consistently increase as we progress from chlorine (Cl) to iodine (I).

Table I. Calculated lattice parameters, bond lengths and formation energies ( $E_f$ ) of  $\text{Rb}_2\text{BX}_6$  ( $\text{B} = \text{Si}, \text{Ge}, \text{Sn}, \text{Pt}$ ;  $\text{X} = \text{Cl}, \text{Br}, \text{I}$ ) VODPs.

Configurations	Lattice parameter ( $a = b = c$ ), $\text{\AA}$		Bond length, $\text{\AA}$		Formation energy ( $E_f$ ) (eV/atom)
	In our study	Previous report	Rb-X	B-X	
$\text{Rb}_2\text{SiCl}_6$	10.12		3.59	2.24	-1.592
$\text{Rb}_2\text{SiBr}_6$	10.71		3.79	2.43	-1.111
$\text{Rb}_2\text{SiI}_6$	11.67		4.13	2.70	-0.926
$\text{Rb}_2\text{GeCl}_6$	10.22		3.62	2.33	-1.403
$\text{Rb}_2\text{GeBr}_6$	10.77		3.81	2.53	-0.983
$\text{Rb}_2\text{GeI}_6$	11.64		4.12	2.78	-0.848
$\text{Rb}_2\text{SnCl}_6$	10.43	10.12[37](b)	3.69	2.47	-1.501
$\text{Rb}_2\text{SnBr}_6$	10.99	10.58[38](a), 11.01[13](b)	3.89	2.65	-1.096
$\text{Rb}_2\text{SnI}_6$	11.81	11.62[39](a), 11.87[13](b)	4.18	2.91	-0.962
$\text{Rb}_2\text{PtCl}_6$	10.21	9.88[40] (a), 10.23[41] (b)	3.61	2.35	-1.257
$\text{Rb}_2\text{PtBr}_6$	10.72	10.72[41] (b)	3.79	2.50	-0.911
$\text{Rb}_2\text{PtI}_6$	11.44	11.22[36](a), 11.54[42] (b)	4.05	2.71	-0.881

a = Experimental reports

b = Theoretical reports

Furthermore, to predict whether these crystals are stable perovskite structures, we examined crystallographic stability. We calculated the Goldschmidt tolerance factor ( $t$ ), octahedral factor ( $\mu$ ), and new tolerance factor ( $\tau$ ) (For details, see Section I of the Supplemental Material). The calculated results indicate that these perovskites remain stable in cubic structures.

## 2. Dynamical Stability:

We employed the DFPT [43] approach to thoroughly assess the dynamical stability of the  $\text{Rb}_2\text{BX}_6$  ( $\text{B} = \text{Si}, \text{Ge}, \text{Sn}, \text{Pt}$ ;  $\text{X} = \text{Cl}, \text{Br}, \text{I}$ ) VODPs. The dynamical stability of a material is a key factor in determining its overall stability as it is closely related to the characteristics of its phonon modes. In the case of  $\text{Rb}_2\text{BX}_6$ , there are 27 phonon modes

linked to its 9 atoms. Among them, 3 are low-frequency vibrations denoted by acoustic mode, while the others are high-frequency vibrations denoted by optical mode. Given that there are no imaginary frequencies for  $\text{Rb}_2\text{SiCl}_6$ ,  $\text{Rb}_2\text{GeCl}_6$ ,  $\text{Rb}_2\text{PtCl}_6$ ,  $\text{Rb}_2\text{SiBr}_6$ ,  $\text{Rb}_2\text{GeBr}_6$ , and  $\text{Rb}_2\text{PtBr}_6$ , indicating these materials appear to be dynamically stable at  $T=0$  K. Rest of the configurations are not dynamically stable at  $T=0$  K. Since there are multiple factors that affect stability, it is more promising to investigate them altogether. Consequently, we extended our investigation to include the examination of mechanical and thermodynamic stability for all the compounds, as detailed in the following sections of this research paper.

### 3. Mechanical Stability and Elastic Properties:

Stability is one of the crucial aspects to consider when choosing a material for its future research applications. Therefore, to acquire a more comprehensive understanding, the mechanical stability and elastic properties of  $\text{Rb}_2\text{BX}_6$  compounds are also investigated alongside the crystallographic and dynamical stability. The mechanical stability and anisotropic behavior of the materials can be described by calculating the elastic constants. We have calculated the second-order elastic constants of 12 VODPs with help of the energy-strain approach[44]. Three distinct elastic constants -  $C_{11}$ ,  $C_{12}$ , and  $C_{44}$  for cubic symmetry are adequate to account for the mechanical stability and anisotropic characteristics of the crystal. We can determine the bulk ( $B$ ), shear ( $G$ ), and Young's ( $Y$ ) moduli, Poisson's Ratio ( $\nu$ ), and Zener Anisotropic Factor ( $A$ ) of materials from these elastic constants (for details, see Section II of the Supplemental Material).

The computed values of  $C_{11}$ ,  $C_{12}$ , and  $C_{44}$  confirm that the elastic constants satisfy the mechanical stability criteria, indicating that these VODPs are mechanically stable (See Table S2). With the use of the VASP package[45], the elastic coefficients ( $C_{ij}$ ) are computed using the GGA-PBE xc functional, and the related bulk modulus ( $B$ ), shear modulus ( $G$ ), Young's modulus ( $Y$ ), and Poisson's ratio ( $\nu$ ) are established using the Voigt-Reuss-Hill technique[46, 47].

The macroscopic capacity of an object to withstand compression under external pressure is described by the bulk modulus ( $B$ ). At the same time, shear modulus ( $G$ ) and Young's modulus ( $Y$ ) describe the shear resistance and stiffness of the material, respectively. In our case,  $\text{Rb}_2\text{GeCl}_6$  has the largest bulk and shear moduli making it the most resistant to compression and shear. Our results show that shear deformation decreases as the X component changes from Cl to I. Similarly, flexibility increases with lower Young's modulus, with iodine-containing materials being more flexible than their Cl and Br counterparts. Next, Poisson ( $\nu$ ) and Pugh ratios ( $B/G$ ) are calculated in order to understand the brittle and ductile characteristics of the materials under consideration. If  $\nu > 0.26$  and  $B/G > 1.75$ , it is recognized that the material is ductile; otherwise, it is brittle[48–50]. From our results, we can conclude that except  $\text{Rb}_2\text{SiCl}_6$ ,  $\text{Rb}_2\text{GeCl}_6$ , and  $\text{Rb}_2\text{PtCl}_6$ , all the other perovskite compounds are ductile and the mentioned three are brittle. Perovskite's ductile quality makes it possible to employ it to create flexible optoelectronic devices. So, we can predict that, except for those three materials, all the other materials can be used for more advanced flexible optoelectronic devices. In addition to the directional characteristics of these materials, we have calculated the Zener anisotropic factor ( $A$ )[51]. The value of  $A$  is equal to 1 for isotropic materials, and any variation from unity in the value of  $A$  indicates that the material has a high degree of anisotropy. Our results reveal that all the considered configurations are anisotropic in nature. After analyzing these 12 different perovskite materials, we find they have different physical and chemical characteristics in various orientations. To make the most of perovskites for things like solar cells and other optoelectronic devices, it's crucial to figure out how to utilize them in real-world scenarios best.

### 4. Thermodynamical Stability:

In assessing the thermodynamic stability of the compounds, the formation energy ( $E_f$ ) is calculated using the following formula:

$$E_f = \frac{E_{\text{Rb}_l\text{B}_m\text{X}_n} - lE_{\text{Rb}} - mE_{\text{B}} - nE_{\text{X}}}{(l + m + n)} \quad (1)$$

where  $E_{\text{Rb}_l\text{B}_m\text{X}_n}$  represents the total energy of investigated compounds and  $E_{\text{Rb}}$ ,  $E_{\text{B}}$ , and  $E_{\text{X}}$  are the energies of individual Rb, B-site (Si, Ge, Sn, Pt) and halogen (Cl, Br, I) atoms in the crystal structure, respectively. Here,  $l$ ,  $m$ ,  $n$  refers to the number of atoms ( $l=2$ ,  $m=1$ ,  $n=6$ ). Exothermic reactions release heat, which is often seen as advantageous for practical synthesis. A negative value of  $E_f$  indicates an exothermic reaction, indicating the possibility of the compound's synthesis. The  $E_f$  values of these VODPs are depicted in Table I. Hence, it can be concluded that the synthesis of these compounds is indeed feasible.

## B. Electronic Properties:

Once we confirmed the stability of the chosen materials, we moved on to the next step to analyze the electronic structure of  $\text{Rb}_2\text{BX}_6$  VODPs, which is crucial for building optoelectronic devices. Initially, GGA-PBE xc functional[30] is used for all computations. We further employed the hybrid HSE06 xc functional[25] and many-body perturbation theory ( $G_0W_0$ ) to calculate the energy bandgaps since PBE functional is well known to underestimate the bandgaps due to the self-interaction error. The spin-orbit coupling (SOC) effects are also taken into account while calculating the electronic properties using the PBE functional. The bandgaps of these 12 combinations are listed in Table II. Estimated bandgap values for different substances in the  $\text{Fm}\bar{3}\text{m}$  phase range from 0.56 eV to 6.12 eV. Four different elements were taken into account in the current study at the B site. Though all elements have a “+4” oxidation state, their valence electron orbitals are arranged differently. This results in variations in their electronic structures, including differences in the arrangement of energy levels and the types of bandgaps.

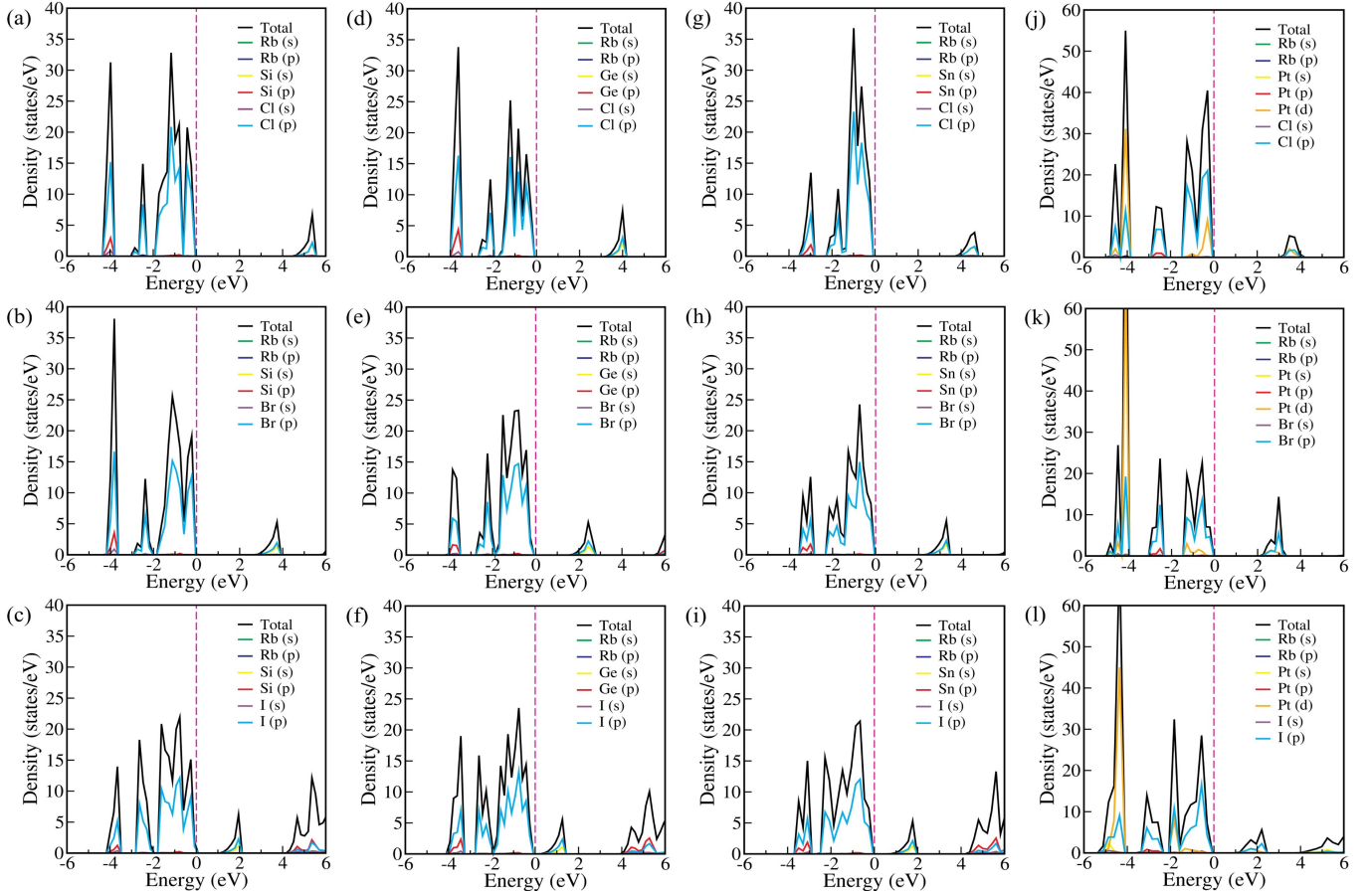


Figure 2. Calculated electronic total density of states (TDOS) and partial density of states (PDOS) of (a-c)  $\text{Rb}_2\text{SiX}_6$ , (d-f)  $\text{Rb}_2\text{GeX}_6$ , (g-i)  $\text{Rb}_2\text{SnX}_6$ , and (j-l)  $\text{Rb}_2\text{PtX}_6$  VODPs using the HSE06 xc functional, where  $X = \text{Cl}, \text{Br}, \text{and I}$ , respectively. The Fermi level is set to be zero and marked by the dashed line.

Calculating bandgaps using PBE and PBE-SOC reveals a slight reduction in the bandgap when SOC is included. The reason for the slight reduction in the bandgap when SOC is included in calculations is the spin mixing induced by SOC, which modifies the electronic states near the band edges, narrowing the bandgap. It changes slightly ( $< 0.1$  eV) when the B-site cation is Si, Ge, and Sn, and when B is Pt, it changes up to 0.26 eV. The calculated bandgap values utilizing PBE and HSE06 functionals are consistent with previously reported theoretical values. In the case of  $\text{Rb}_2\text{SnI}_6$ , the energy bandgap value also agrees with previously reported experimental data. Figure 3 shows the electronic band structures of  $\text{Rb}_2\text{BX}_6$ , computed using the  $G_0W_0@PBE$  technique. Except for  $\text{Rb}_2\text{PtI}_6$  and  $\text{Rb}_2\text{PtBr}_6$ , all of the compounds have a direct bandgap. Across all cases, there’s a consistent trend: the bandgap values follow the order  $\text{I} < \text{Br} < \text{Cl}$ . This trend can be explained with the help of Pauling electronegativity[52]. According to Pauling, the electronegativity values for halogen atoms are in the order of  $\text{I} (2.66) < \text{Br} (2.96) < \text{Cl} (3.16)$ . A higher

electronegativity of the halogen atom results in stronger bond interactions between the halogen and B-site atoms, leading to an upward shift in the conduction band, and consequently, larger bandgaps.

Table II. Computed bandgap ( $E_g$ ) of  $\text{Rb}_2\text{BX}_6$  (B = Si, Ge, Sn, Pt; X = Cl, Br, I) VODPs using the PBE/PBE-SOC, HSE06 xc-functionals, and  $\text{G}_0\text{W}_0$ @PBE method.

Configurations	$E_g$ (eV)			Nature	Previous reports of $E_g$ (eV)	
	PBE/PBE-SOC	HSE06	$\text{G}_0\text{W}_0$ @PBE		Theoretical	Experimental
$\text{Rb}_2\text{SiCl}_6$	3.21/3.18	4.58	6.12	D	4.57[53](b)	
$\text{Rb}_2\text{SiBr}_6$	1.64/1.55	2.74	3.66	D	2.72[53](b)	
$\text{Rb}_2\text{SiI}_6$	0.28/0.21	1.08	1.82	D	0.96[53](b)	
$\text{Rb}_2\text{GeCl}_6$	2.04/2.02	3.37	4.76	D		
$\text{Rb}_2\text{GeBr}_6$	0.72/0.66	1.76	2.42	D		
$\text{Rb}_2\text{GeI}_6$	0.01/–	0.33	0.56	D	1.24[54](c)	
$\text{Rb}_2\text{SnCl}_6$	2.54/2.52	3.87	5.25	D	2.40[55](a) 3.85[56]	
$\text{Rb}_2\text{SnBr}_6$	1.30/1.22	2.37	3.38	D	1.30 [13](a), 2.17[13] (b)	
$\text{Rb}_2\text{SnI}_6$	0.03/0.01	0.80	1.16	D	0.12[13] (a), 1.10 [13] (b) 1.32[57]	
$\text{Rb}_2\text{PtCl}_6$	1.97/1.71	3.30	4.35	D	3.39[58](c)	
$\text{Rb}_2\text{PtBr}_6$	1.28/1.17	2.26	3.18	I	1.30[18] (b)	
$\text{Rb}_2\text{PtI}_6$	0.46/0.34	1.19	1.76	I	1.15 [14](b)	

a = PBE  
b = HSE06  
c = TB-mBJ

To obtain more band information, we analyze the total density of states (TDOS) and projected density of electronic states (PDOS) using HSE06 xc functional. The compounds having a direct bandgap, the VBM and CBM are both found at point  $\Gamma$ . The CBM consists of  $s$  orbitals of B-site cation (Si, Ge, Sn) and  $p$  orbitals of halogen atom (Cl, Br, I), while the VBM is comprised only  $p$  orbitals of halogen atom. However, for  $\text{Rb}_2\text{PtCl}_6$ , the VBM and CBM are located at a different point X, with a direct bandgap of 4.35 eV. Here, contributions to the VBM and CBM come from Cl- $p$  and Pt- $d$  orbitals. Figure 2 shows the TDOS and PDOS of all the elements.  $\text{Rb}_2\text{PtBr}_6$  and  $\text{Rb}_2\text{PtI}_6$  exhibit indirect bandgaps, with the CBM and VBM located at the X and  $\Gamma$  points, respectively. Based on the PDOS calculations, in  $\text{Rb}_2\text{PtBr}_6$ , VBM is mainly comprised Br- $p$  orbitals and CBM is dominated by Br- $p$  orbitals with a small contribution from Pt- $d$  orbitals. Similarly, in  $\text{Rb}_2\text{PtI}_6$ , the VBM consists mainly of I- $p$  orbitals, and the CBM is also primarily composed of I- $p$  orbitals, with a minor contribution from Pt- $d$  orbitals. Overall, the  $\text{Rb}_2\text{BX}_6$  compounds demonstrate significant potential for optoelectronic applications, with their bandgaps covering the infrared to ultraviolet range. Particularly,  $\text{Rb}_2\text{SnI}_6$  stands out as the most suitable one for photovoltaic applications, owing to its direct bandgap of 1.16 eV, which falls within the optimal range for solar cell performance.

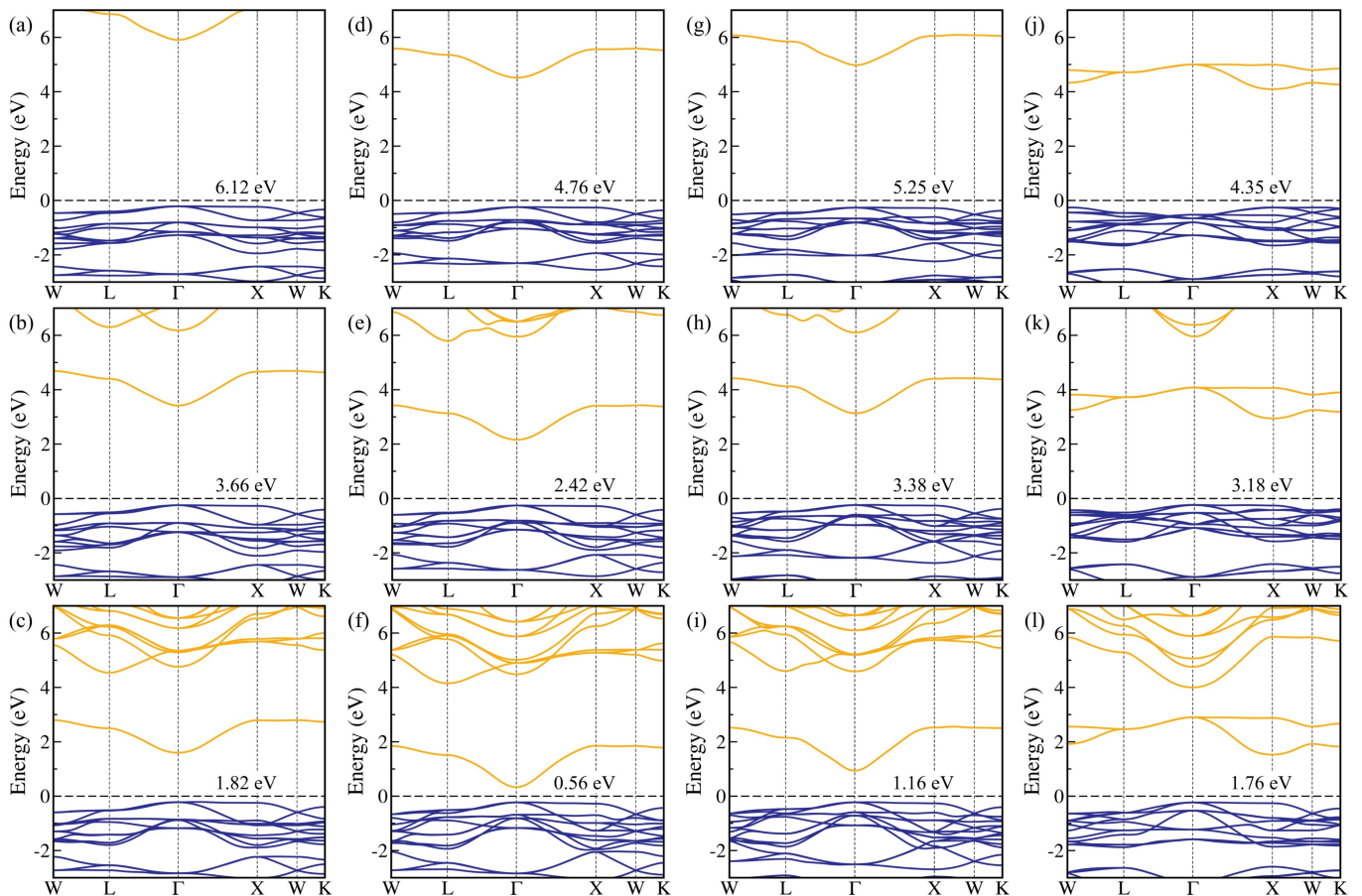


Figure 3. Calculated electronic band structures of (a-c)  $\text{Rb}_2\text{SiX}_6$ , (d-f)  $\text{Rb}_2\text{GeX}_6$ , (g-i)  $\text{Rb}_2\text{SnX}_6$ , and (j-l)  $\text{Rb}_2\text{PtX}_6$  VODPs using the  $G_0W_0@PBE$  method, where  $X = \text{Cl}, \text{Br}, \text{I}$ , respectively. The Fermi level is set to be zero and marked by the dashed line.

To comprehend carrier transport behavior, we computed the effective masses of charge carriers at the band edges of the aforementioned systems. We derive the second-order derivative from the E-k dispersion curve near the band edges using the equation  $m^* = \hbar^2 [\partial^2 E(k)/\partial k^2]^{-1}$ , where  $m^*$  represents the effective mass,  $\hbar$  denotes the reduced Planck's constant,  $E(k)$  signifies the energy eigenvalue, and  $k$  stands for the wave vector. The effective masses of electrons and holes are linked to the dispersion of the CBM and VBM. Greater curvature in the CBM and VBM corresponds to lighter effective masses. From the effective mass values presented in Table III, we observe the electron effective masses tend to be lower than their corresponding hole effective masses. This is primarily attributed to the pronounced dispersive characteristics of the CBM compared to the VBM, as evident from the band structures illustrated in Figure 3. The heavier hole masses, indicating  $\text{Rb}_2\text{BX}_6$  VODPs are more suitable for  $n$ -type semiconductors.

Table III. Carrier's effective mass, and reduced mass ( $\mu^*$ ) of  $\text{Rb}_2\text{BX}_6$  ( $B = \text{Si}, \text{Ge}, \text{Sn}, \text{Pt}$ ;  $X = \text{Cl}, \text{Br}, \text{I}$ ) VODPs calculated using  $G_0W_0@PBE$  method. Here,  $m_e$  and  $m_h$  represents electron and hole effective mass (where  $m_0$  is the rest mass of the electron), respectively. The bold values provided in parentheses are the effective mass and reduced mass at direct band edge.

Configurations	$m_e (m_0)$	$m_h (m_0)$	$\mu^* (m_0)$	Configurations	$m_e (m_0)$	$m_h (m_0)$	$\mu^* (m_0)$
$\text{Rb}_2\text{SiCl}_6$	0.641	1.527	0.451	$\text{Rb}_2\text{SnCl}_6$	0.580	1.392	0.409
$\text{Rb}_2\text{SiBr}_6$	0.471	1.046	0.325	$\text{Rb}_2\text{SnBr}_6$	0.390	0.993	0.280
$\text{Rb}_2\text{SiI}_6$	0.330	0.743	0.229	$\text{Rb}_2\text{SnI}_6$	0.186	0.682	0.146
$\text{Rb}_2\text{GeCl}_6$	0.622	1.411	0.432	$\text{Rb}_2\text{PtCl}_6$	0.831	2.045	0.591
$\text{Rb}_2\text{GeBr}_6$	0.383	0.987	0.276	$\text{Rb}_2\text{PtBr}_6$	0.559	0.997 ( <b>0.906</b> )	0.358 ( <b>0.346</b> )
$\text{Rb}_2\text{GeI}_6$	0.268	0.687	0.193	$\text{Rb}_2\text{PtI}_6$	0.372	0.662 ( <b>0.681</b> )	0.238 ( <b>0.241</b> )

### C. Optical Properties:

Conducting a thorough investigation into the optical properties of a material, including its dielectric function and absorption coefficient, is fundamental for gaining a comprehensive understanding of its viability for optoelectronic applications. In our contribution, the real  $[\text{Re}(\epsilon)]$  and imaginary  $[\text{Im}(\epsilon)]$  part of the frequency-dependent dielectric function are calculated to study the optical characteristics of the chosen VODPs. The real part of the complex dielectric function indicates how a material responds to an electric field, while the imaginary part tells us how much of the light's energy is being consumed as it passes through the material. To improve the accuracy of our predictions, we employed the MBPT-based GW-BSE method, which explicitly considers electron-hole interaction[33, 34].

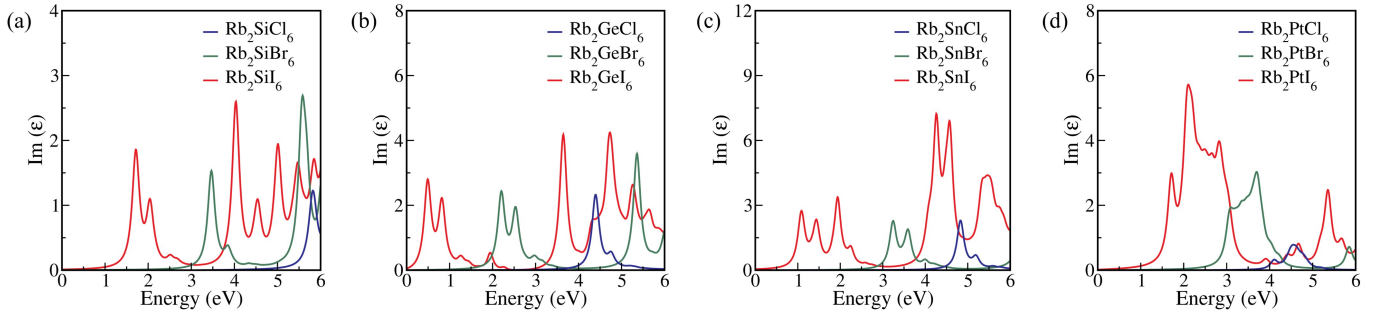


Figure 4. Imaginary  $[\text{Im}(\epsilon)]$  part of the dielectric function of (a)  $\text{Rb}_2\text{SiX}_6$ , (b)  $\text{Rb}_2\text{GeX}_6$ , (c)  $\text{Rb}_2\text{SnX}_6$ , and (d)  $\text{Rb}_2\text{PtX}_6$  VODPs, where  $X = \text{Cl}, \text{Br}, \text{and I}$ , respectively, obtained using the BSE@ $G_0W_0$ @PBE method.

The computed imaginary parts of the dielectric function are plotted in Figure 4. The first absorption peak appears in the range 0.490–5.822 eV. This primarily occurs due to the shift from  $X-p$  orbitals at the upper edge of the valence band to the blending of  $B-s$  and  $X-p$  orbitals hybridization states in the CBM. The optical characteristics of  $\text{Rb}_2\text{BX}_6$  compounds display comparable patterns, with the initial peak positions varying based on distinct bandgap values. As the bandgap increases, we notice that the edges of the absorption spectra tend to shift towards the blue end. It's interesting to note that materials with indirect bandgaps have absorption edges significantly higher than their electronic bandgaps, while those with direct bandgaps have absorption edges closer to their electronic bandgaps. This suggests that in direct-band-gap materials, the first optical transition occurs between the VBM and the CBM, unlike in indirect-band-gap materials. Absorption-edge values derived from the BSE@ $G_0W_0$ @PBE method fall within the 0.31-5.58 eV range, suggesting that these materials absorb light spanning from the infrared to the ultraviolet region. In conclusion, materials with absorption spanning the infrared to ultraviolet regions present versatile optoelectronic properties, offering potential for enhanced efficiency and performance across a wide range of applications. This highlights the promise of  $\text{Rb}_2\text{BX}_6$  compounds for various optoelectronic applications spanning diverse device types.

### D. Excitonic Properties:

An exciton is a quasiparticle consisting of an electron and a hole bound together by electrostatic forces. The electron and hole can form a pair that behaves like a single, composite particle due to their mutual attraction. The energy required to split the exciton into an electron and a hole is defined as the exciton binding energy, which is another crucial factor in photovoltaic applications. The lower the exciton binding energy, the more easily the electron and hole can be separated, which results in higher photoelectric conversion efficiency. In our study, the exciton binding energy is calculated using the Wannier-Mott (WM)[59] formula given below:

$$E_B = \left( \frac{\mu^*}{m_0 \epsilon_{\text{eff}}^2} \right) R_{\infty}, \quad (2)$$

here  $\mu^*$ ,  $m_0$ ,  $\epsilon_{\text{eff}}$ , and  $R_{\infty}$  stand for the reduced mass of charge carriers, rest mass of the electron, effective dielectric constant and Rydberg constant respectively.  $\mu^*$  is given by

$$\frac{1}{\mu^*} = \frac{1}{m_e^*} + \frac{1}{m_h^*} \quad (3)$$

In the case of  $\text{Rb}_2\text{PtBr}_6$  and  $\text{Rb}_2\text{PtI}_6$ , which have an indirect bandgap, we calculated the reduced mass ( $\mu^*$ ) of carriers by focusing on their lowest direct band edges (look at Table III).

To calculate the exciton binding energy ( $E_B$ ), we need  $\varepsilon_{\text{eff}}$ . If  $E_B \ll \hbar\omega_{LO}$ , lattice relaxation must be considered, and an intermediate dielectric constant between  $\varepsilon_\infty$  and  $\varepsilon_{\text{static}}$  should be used. However, when  $E_B \gg \hbar\omega_{LO}$ , as in our case, the ionic contribution becomes negligible, and the effective dielectric constant ( $\varepsilon_{\text{eff}}$ ) approaches  $\varepsilon_\infty$ , meaning the dielectric screening is dominated by the electronic contribution[60].

We employed the density functional perturbation theory (DFPT) method to estimate the ionic contribution to the dielectric function ( $\varepsilon_{\text{ion}}$ ), and the electronic contribution ( $\varepsilon_\infty$ ) is estimated using BSE@G<sub>0</sub>W<sub>0</sub>@PBE method (for details, see the Table S4). The upper ( $E_{Bu}$ ) and lower ( $E_{Bl}$ ) bound to the exciton binding energy is computed from the contribution of optical ( $\varepsilon_\infty$ ) and static ( $\varepsilon_{\text{static}}$ ) dielectric constants, respectively. The  $E_{Bu}$  and  $E_{Bl}$  values calculated using the WM method are depicted in Table S4.  $E_{Bu}$  and  $E_{Bl}$  show a noticeable decrease in double perovskite compounds when moving from Cl to I -compositions. This decline is attributed to the higher dielectric constant of I-containing compounds compared to their Cl and Br counterparts. Additionally, the upper and lower limits of  $E_B$  suggest that the electronic contribution plays a more significant role than the ionic contribution in the dielectric screening of these VODPs.

In addition to the WM model, we extended our analysis by calculating the  $E_B$  for  $\text{Rb}_2\text{BX}_6$  systems using the standard BSE@G<sub>0</sub>W<sub>0</sub>@PBE method[61, 62]. The formula used for this calculation is  $E_B = E_g^{\text{dir}} - E_o$ , where  $E_g^{\text{dir}}$  represents the GW (direct) bandgap, and  $E_o$  corresponds to the position of the first strong absorption peak from BSE calculation. This approach provides a more comprehensive assessment of exciton binding energy. In I-containing compounds, BSE@G<sub>0</sub>W<sub>0</sub>@PBE and WM methods yield similar  $E_B$  values, while the WM model predicts stronger localized resonant excitons for Cl and Br-containing systems ranging from 0.072 to 0.682 eV. Thus, the electronic contribution dominates over the ionic contribution in dielectric screening for I-containing VODPs.

Table IV. Excitonic parameters of  $\text{Rb}_2\text{BX}_6$  (B = Si, Ge, Sn, Pt; X = Cl, Br, I) VODPs. Here,  $E_g^{\text{dir}}$  is the direct G<sub>0</sub>W<sub>0</sub>@PBE bandgap (in unit eV),  $E_o$  represents the exciton energy (in unit eV),  $E_B$  represents the exciton binding energy (in unit eV),  $\Delta E_B^{\text{ph}}$  is the phonon screening corrections of exciton binding energy (in unit meV),  $(E_B + \Delta E_B^{\text{ph}})$  is the corrected values of exciton binding energy (in unit eV),  $r_{\text{exc}}$  is the exciton radius (in unit nm), and  $|\phi_n(0)|^2$  is the probability of a wavefunction for electron-hole pair at zero separation (in unit  $m^{-3}$ ).

Configurations	$E_g^{\text{dir}}$ (eV)	$E_o$ (eV)	$E_B$ (eV)	$\Delta E_B^{\text{ph}}$ (meV)	$(E_B + \Delta E_B^{\text{ph}})$ (eV)	$r_{\text{exc}}$ (nm)	$ \phi_n(0) ^2$ ( $10^{28}m^{-3}$ )
$\text{Rb}_2\text{SiCl}_6$	6.122	5.822	0.300	-15.70	0.284	0.352	0.731
$\text{Rb}_2\text{SiBr}_6$	3.664	3.467	0.197	-12.85	0.184	0.555	0.186
$\text{Rb}_2\text{SiI}_6$	1.820	1.712	0.108	-10.30	0.098	1.107	0.023
$\text{Rb}_2\text{GeCl}_6$	4.763	4.402	0.361	-13.22	0.348	0.298	1.208
$\text{Rb}_2\text{GeBr}_6$	2.419	2.205	0.214	-9.23	0.205	0.594	0.152
$\text{Rb}_2\text{GeI}_6$	0.561	0.490	0.071	-6.20	0.065	1.656	0.007
$\text{Rb}_2\text{SnCl}_6$	5.245	4.825	0.420	-12.66	0.407	0.310	1.064
$\text{Rb}_2\text{SnBr}_6$	3.379	3.247	0.132	-8.73	0.123	0.546	0.196
$\text{Rb}_2\text{SnI}_6$	1.164	1.090	0.074	-6.70	0.067	1.399	0.012
$\text{Rb}_2\text{PtCl}_6$	4.353	4.112	0.241	-10.35	0.231	0.251	2.022
$\text{Rb}_2\text{PtBr}_6$	3.204	3.096	0.108	-6.12	0.102	0.547	0.194
$\text{Rb}_2\text{PtI}_6$	1.786	1.710	0.076	-4.17	0.072	1.098	0.024

In a recent study, Filip and collaborators[63] presented a discussion on phonon screening into the calculation of exciton binding energy. They assumed isotropic, parabolic electronic band dispersion and considered four material parameters such as reduced effective mass, static and optical dielectric constants, and the frequency of the longitudinal optical phonon mode ( $\omega_{LO}$ ). We determined the characteristic frequency  $\omega_{LO}$  using the athermal "B" scheme proposed by Hellwarth et al.[64], which involves considering the spectral average of infrared-active optical phonon modes (for details, see the Supplemental Material). The correction due to phonon screening is expressed as[63]:

$$\Delta E_B^{\text{ph}} = -2\omega_{LO} \left( 1 - \frac{\varepsilon_\infty}{\varepsilon_{\text{static}}} \right) \frac{\sqrt{1 + \omega_{LO}/E_B} + 3}{\left( 1 + \sqrt{1 + \omega_{LO}/E_B} \right)^3} \quad (4)$$

According to Table IV, phonon screening leads to a decrease in the exciton binding energy by 3.01 % to 9.54 %. While phonon screening does reduce the exciton binding energy, the effect is not particularly significant. This suggests that for VODPs, electronic contribution plays a more dominant role in dielectric screening compared to ionic or phonon contributions.

Further, using dielectric constant ( $\varepsilon_{\text{eff}}$ ) and reduced mass of the charge carriers ( $\mu^*$ ), we calculated several excitonic properties such as excitonic radius ( $r_{exc}$ ), exciton lifetime ( $\tau_{exc}$ ) and the probability of a wavefunction ( $|\phi_n(0)|^2$ ) for electron-hole pair at zero separation.  $|\phi_n(0)|^2$  is determined using the following formula[59],

$$|\phi_n(0)|^2 = \frac{1}{\pi(r_{exc})^3 n^3} \quad (5)$$

where  $r_{exc}$  is the exciton radius, and  $n$  is the exciton energy level. In order to evaluate  $|\phi_n(0)|^2$ , first we determined excitonic radius ( $r_{exc}$ ) by the given formula[59]

$$r_{exc} = \frac{m_0}{\mu^*} \varepsilon_{\text{eff}} n^2 r_{Ry}, \quad (6)$$

here,  $m_0$  is the rest mass of the electron,  $\mu^*$  is the reduced mass of charge carriers,  $\varepsilon_{\text{eff}}$  is the effective dielectric constant,  $n$  is the exciton energy level ( $n=1$  gives the smallest exciton radius) and  $r_{Ry}$  is the Bohr radius (0.0529 nm). In this scenario, the electronic contribution to the dielectric function ( $\varepsilon_{\infty}$ ) is regarded as the effective value due to the insignificance of the ionic contribution to dielectric screening. The exciton lifetime ( $\tau_{exc}$ ) is inversely proportional to the probability of a wavefunction ( $|\phi_n(0)|^2$ ) for electron-hole pair at zero separation (for details, for details, see Section IV of the Supplemental Material). All the values of  $|\phi_n(0)|^2$  are given in Table IV, which suggests that exciton lifetime keeps increasing while going from Cl to I-containing systems, and I-containing compounds have longer exciton lifetime. A prolonged exciton lifetime suggests reduced carrier recombination, leading to increased conversion efficiency that is beneficial for photovoltaic applications.

### E. Polaronic Properties:

Understanding polaronic parameters holds significant promise for advancing material design and technology. The Fröhlich mesoscopic model[65] reveals insights into the impact of longitudinal optical phonon modes on carrier mobility, consequently improving device performance. According to this model, the charge carriers moving through the lattice interact with the polar optical phonons, and the interaction is given by the dimensionless Fröhlich parameter  $\alpha$  as follows:

$$\alpha = \left( \frac{1}{\varepsilon_{\infty}} - \frac{1}{\varepsilon_{\text{static}}} \right) \sqrt{\frac{R_{\infty}}{ch\omega_{LO}}} \sqrt{\frac{m^*}{m_e}} \quad (7)$$

where,  $\varepsilon_{\infty}$  and  $\varepsilon_{\text{static}}$  represent the electronic and static dielectric constants, respectively. Meanwhile,  $h$  stands for Planck's constant,  $c$  denotes the speed of light, and  $R_{\infty}$  is Rydberg's constant. Notably,  $\alpha \ll 1$  typically signifies weak electron (hole) -phonon coupling, whereas  $\alpha > 10$  denotes strong coupling[65]. From the  $\alpha$  values depicted in Table V, we find an intermediate electron (hole)-phonon coupling (1.66–9.68) for our configurations. Additionally, Debye temperature ( $\theta_D$ ) plays a key role in determining carrier-phonon interactions. A lower  $\theta_D$  relative to room temperature significantly strengthens carrier-phonon coupling, enhancing polaronic effects. In our study, most systems exhibit  $\theta_D$  values lower than room temperature, indicating significant carrier-phonon interactions and increased polaronic contributions.

Using the values of  $\alpha$ , we can ascertain the decrease in the quasiparticle (QP) gap resulting from polaron formation through the following equation. Following equation describes the reduction in QP energy for both electrons and holes[60, 66],

$$E_p = (-\alpha - 0.0123\alpha^2)\hbar\omega_{LO} \quad (8)$$

here,  $E_p$  is the polaron energy. For our systems Rb<sub>2</sub>SiCl<sub>6</sub>, Rb<sub>2</sub>SiBr<sub>6</sub>, Rb<sub>2</sub>SiI<sub>6</sub>, Rb<sub>2</sub>GeCl<sub>6</sub>, Rb<sub>2</sub>GeBr<sub>6</sub>, Rb<sub>2</sub>GeI<sub>6</sub>, Rb<sub>2</sub>SnCl<sub>6</sub>, Rb<sub>2</sub>SnBr<sub>6</sub>, Rb<sub>2</sub>SnI<sub>6</sub>, Rb<sub>2</sub>PtCl<sub>6</sub>, Rb<sub>2</sub>PtBr<sub>6</sub>, and Rb<sub>2</sub>PtI<sub>6</sub>, the QP gap is lowered by 0.257, 0.173, 0.097, 0.306, 0.158, 0.052, 0.318, 0.184, 0.095, 0.26, 0.113, and 0.52 eV, respectively. Upon comparison of these values with  $E_B$  given in Table IV, we can conclude that the charge-separated polaronic state is less stable than the bound exciton except Rb<sub>2</sub>SnBr<sub>6</sub>, Rb<sub>2</sub>SnI<sub>6</sub>, Rb<sub>2</sub>PtCl<sub>6</sub>, and Rb<sub>2</sub>PtBr<sub>6</sub>. Additionally, effective polaron masses ( $m_p$ ) are calculated by Feynman extended Fröhlich's polaron theory[67]:

$$m_p = m^* \left( 1 + \frac{\alpha}{6} + \frac{\alpha^2}{40} + \dots \right) \quad (9)$$

where,  $m^*$  stands for effective mass calculated from bandstructure calculations. This expression indicates that the polaron mass consistently surpasses the effective mass obtained from band structure calculations, thereby impacting charge carrier mobilities.

Next, we calculated Polaron mobilities ( $\mu_p$ ) defined for electron and hole with the help of the Hellwarth polaron model[64]:

$$\mu_p = \frac{(3\sqrt{\pi}e)}{2\pi c\omega_{LO}m^*\alpha} \frac{\sinh(\beta/2)}{\beta^{5/2}} \frac{w^3}{v^3} \frac{1}{K} \quad (10)$$

where,  $\beta = hc\omega_{LO}/k_B T$ ,  $e$  represents the electronic charge,  $m^*$  denotes the effective mass of the charge carrier, and  $w$  and  $v$  are associated with temperature-dependent variational parameters (for details, see the Supplemental Material).  $K$  is defined as follows:

$$K(a, b) = \int_0^\infty du [u^2 + a^2 - b \cos(vu)]^{-3/2} \cos(u) \quad (11)$$

Here,  $a^2$  and  $b$  are evaluated as:

$$a^2 = (\beta/2)^2 + \frac{(v^2 - w^2)}{w^2 v} \beta \coth(\beta v/2) \quad (12)$$

$$b = \frac{v^2 - w^2}{w^2 v} \frac{\beta}{\sinh(\beta v/2)} \quad (13)$$

The data presented in Table V reveals that systems having iodine (I) exhibit higher polaron mobility compared to those containing bromine (Br) and chlorine (Cl). This difference could be attributed to variations in the electronegativity among different halogens. Hence, it can be inferred that compounds containing iodine may serve as more effective charge transport materials. The significant difference in polaron mobility between electrons (3.33–85.11  $\text{cm}^2\text{V}^{-1}\text{s}^{-1}$ ) and holes (0.34–17.98  $\text{cm}^2\text{V}^{-1}\text{s}^{-1}$ ) further supports the characterization of  $\text{Rb}_2\text{BX}_6$  as an n-type semiconductor. In contrast, the electron polaron mobility for Cs-based VODPs ranges from 42.15–71.12  $\text{cm}^2\text{V}^{-1}\text{s}^{-1}$ [68], while for Rb-based VODPs, it reaches up to 85.11  $\text{cm}^2\text{V}^{-1}\text{s}^{-1}$ . This difference highlights the superior charge transport capabilities of our materials compared to previously studied Cs-based VODPs.

Table V. Polaron parameters corresponding to electrons ( $e$ ) and holes ( $h$ ) in  $\text{Rb}_2\text{BX}_6$  (B = Si, Ge, Sn, Pt; X = Cl, Br, I) VODPs. Here,  $\omega_{LO}$  represents the characteristic phonon angular frequency (in unit THz),  $\theta_D$  represents debye temperature (in unit K),  $\alpha$  represents Fröhlich interaction parameter,  $m_p$  represents effective mass of the polaron (in terms of  $m^*$ ),  $E_p$  represents polaron energy (in unit meV), and  $\mu_p$  represents the polaron mobility (in unit  $\text{cm}^2\text{V}^{-1}\text{s}^{-1}$ ), respectively.

Configurations	$\omega_{LO}$ (THz)	$\theta_D$ (K)	$\alpha$		$m_p/m^*$		$E_p$ (meV)		$\mu_p$ ( $\text{cm}^2\text{V}^{-1}\text{s}^{-1}$ )	
			$e$	$h$	$e$	$h$	$e$	$h$	$e$	$h$
$\text{Rb}_2\text{SiCl}_6$	7.06	339	3.28	5.06	1.82	2.48	99.77	157.15	9.01	1.53
$\text{Rb}_2\text{SiBr}_6$	5.76	277	2.78	4.15	1.66	2.12	68.58	104.05	17.40	3.85
$\text{Rb}_2\text{SiI}_6$	4.31	207	2.10	3.16	1.46	1.78	38.45	58.59	42.25	10.29
$\text{Rb}_2\text{GeCl}_6$	5.12	246	5.31	8.00	2.59	3.93	119.94	186.32	4.07	0.56
$\text{Rb}_2\text{GeBr}_6$	3.74	180	3.68	5.92	1.95	2.86	59.58	98.37	16.87	2.57
$\text{Rb}_2\text{GeI}_6$	2.88	138	1.66	2.66	1.35	1.62	20.20	32.76	85.11	17.98
$\text{Rb}_2\text{SnCl}_6$	4.37	210	6.25	9.68	3.02	4.96	121.80	196.04	3.33	0.34
$\text{Rb}_2\text{SnBr}_6$	3.09	148	5.09	8.13	2.50	4.01	69.21	114.44	10.54	1.36
$\text{Rb}_2\text{SnI}_6$	2.29	110	3.23	6.18	1.80	2.99	31.85	63.06	57.81	5.28
$\text{Rb}_2\text{PtCl}_6$	4.40	211	5.11	8.02	2.50	3.94	98.96	160.55	3.72	0.45
$\text{Rb}_2\text{PtBr}_6$	2.92	140	3.79	5.07	1.99	2.49	47.97	65.13	12.91	4.35
$\text{Rb}_2\text{PtI}_6$	2.11	101	2.46	3.28	1.56	1.82	22.15	29.82	44.04	16.74

#### IV. CONCLUSIONS:

In summary, our investigation into  $\text{Rb}_2\text{BX}_6$  systems unveils their adherence to the standard cubic double-perovskite lattice [space group  $\text{Fm}\bar{3}\text{m}$  (225)], along with maintaining ideal tolerance and octahedral factors, as per the crystallographic stability criterion. Additionally, the negative formation energies indicate the phase stability of these systems. Moreover, our analysis demonstrates their mechanical stability and elastic characteristics, revealing their flexible and ductile nature, accompanied by elastic anisotropy. Employing GW-based electronic band-structure calculations, we anticipate a broad tunability of the bandgap within the range of 0.56 to 6.12 eV for direct bandgap materials and 1.76 to 3.18 eV for indirect bandgap materials. Notably, incorporating halogen atoms results in varied band-gap values, with Cl-containing compounds exhibiting larger bandgaps than their Br and I-containing counterparts. Furthermore, our findings indicate the absorption-edge values fall within the range of 0.31–5.58 eV, enabling efficient light absorption from infrared to ultraviolet wavelengths. Remarkably, these materials exhibit low carrier effective masses, suggesting exceptional charge-carrier mobility and lighter electron masses, indicating these materials are more suitable for n-type semiconductors. Excitonic properties indicates low to moderate exciton-binding energies and varying exciton lifetimes, suggesting the potential for higher quantum yield and conversion efficiency. Finally, investigating polaronic properties unveils enhanced polaron mobility (ranging from 3.33 to 85.11  $\text{cm}^2\text{V}^{-1}\text{s}^{-1}$  for electrons) than the previously reported VODPs materials. Additionally, a comparison between polaron energy and exciton binding energy indicates a less stable state for charge-separated polarons except  $\text{Rb}_2\text{SnBr}_6$ ,  $\text{Rb}_2\text{SnI}_6$ ,  $\text{Rb}_2\text{PtCl}_6$ , and  $\text{Rb}_2\text{PtBr}_6$ . Collectively, our study underscores the potential of  $\text{Rb}_2\text{BX}_6$  VODP compounds in various optoelectronic applications, owing to their versatile properties.

#### ACKNOWLEDGMENTS

S.A. would like to acknowledge the Council of Scientific and Industrial Research (CSIR), Government of India [Grant No. 09/1128(11453)/2021-EMR-I] for Senior Research Fellowship. A.C. would also like to acknowledge the Shiv Nadar Foundation for financial support. The authors acknowledge the High Performance Computing Cluster (HPCC) ‘Magus’ at Shiv Nadar Institution of Eminence for providing computational resources that have contributed to the research results reported within this paper.

- 
- [1] M. Hussain, M. Rashid, A. Ali, M. F. Bhopal, and A. Bhatti, *Ceram. Int.* **46**, 21378 (2020).
  - [2] K. A. Bush, A. F. Palmstrom, Z. J. Yu, M. Boccard, R. Checharoen, J. P. Mailoa, D. P. McMeekin, R. L. Z. Hoye, C. D. Bailie, T. Leijtens, I. M. Peters, M. C. Minichetti, N. Rolston, R. Prasanna, S. Sofia, D. Harwood, W. Ma, F. Moghadam, H. J. Snaith, T. Buonassisi, Z. C. Holman, S. F. Bent, and M. D. McGehee, *Nat. Energy* **2**, 17009 (2017).
  - [3] M. K. Jana, S. M. Janke, D. J. Dirkes, S. Dovletgeldi, C. Liu, X. Qin, K. Gundogdu, W. You, V. Blum, and D. B. Mitzi, *J. Am. Chem. Soc.* **141**, 7955 (2019), pMID: 31017429, <https://doi.org/10.1021/jacs.9b02909>.
  - [4] S. Adhikari and P. Johari, *Phys. Rev. Mater.* **7**, 075401 (2023).
  - [5] S. Nazir, S. Maqsood, N. Noor, S. Mumtaz, and I. M. Moussa, *Polyhedron* **256**, 117003 (2024).
  - [6] W. Zhang, G. E. Eperon, and H. J. Snaith, *Nat. Energys* **1**, 16048 (2016).
  - [7] W.-J. Yin, T. Shi, and Y. Yan, *Adv. Mater.* **26**, 4653 (2014), <https://onlinelibrary.wiley.com/doi/pdf/10.1002/adma.201306281>.
  - [8] A. A. Dotsenko, V. I. Vovna, V. V. Korochentsev, A. G. Mirochnik, O. L. Shcheka, T. V. Sedakova, and V. I. Sergienko, *Inorg. Chem.* **58**, 6796 (2019), <https://doi.org/10.1021/acs.inorgchem.9b00250>.
  - [9] A. E. Maughan, A. M. Ganose, M. M. Bordelon, E. M. Miller, D. O. Scanlon, and J. R. Neilson, *J. Am. Chem. Soc.* **138**, 8453 (2016), pMID: 27284638, <https://doi.org/10.1021/jacs.6b03207>.
  - [10] M. M. S. Karim, A. M. Ganose, L. Pieters, W. W. Winnie Leung, J. Wade, L. Zhang, D. O. Scanlon, and R. G. Palgrave, *Chem. Mater.* **31**, 9430 (2019), pMID: 32116409, <https://doi.org/10.1021/acs.chemmater.9b03267>.
  - [11] W. Travis, E. N. K. Glover, H. Bronstein, D. O. Scanlon, and R. G. Palgrave, *Chem. Sci.* **7**, 4548 (2016).
  - [12] M. Faizan, J. Xie, G. Murtaza, C. Echeverría-Arondo, T. Alshahrani, K. C. Bhamu, A. Laref, I. Mora-Seró, and S. Haidar Khan, *Phys. Chem. Chem. Phys.* **23**, 4646 (2021).
  - [13] M. Faizan, K. C. Bhamu, G. Murtaza, X. He, N. Kulhari, M. M. AL-Anazy, and S. H. Khan, *Sci. Rep.* **11**, 6965 (2021).
  - [14] X.-H. Zhao, X.-N. Wei, T.-Y. Tang, L.-K. Gao, Q. Xie, L.-M. Lu, and Y.-L. Tang, *Opt. Mater.* **114**, 110952 (2021).
  - [15] H.-M. Huang, Z.-Y. Jiang, and S.-J. Luo, *Chin. Phys. B* **26**, 096301 (2017).
  - [16] B. Lee, C. C. Stoumpos, N. Zhou, F. Hao, C. Malliakas, C.-Y. Yeh, T. J. Marks, M. G. Kanatzidis, and R. P. H. Chang, *J. Am. Chem. Soc.* **136**, 15379 (2014), pMID: 25299304, <https://doi.org/10.1021/ja508464w>.
  - [17] M.-G. Ju, M. Chen, Y. Zhou, H. F. Garces, J. Dai, L. Ma, N. P. Padture, and X. C. Zeng, *ACS Energy Lett.* **3**, 297 (2018), <https://doi.org/10.1021/acsenerylett.7b01167>.

- [18] Y. Cai, W. Xie, H. Ding, Y. Chen, K. Thirumal, L. H. Wong, N. Mathews, S. G. Mhaisalkar, M. Sherburne, and M. Asta, *Chem. Mater.* **29**, 7740 (2017), <https://doi.org/10.1021/acs.chemmater.7b02013>.
- [19] L. Zhou, J.-F. Liao, Z.-G. Huang, X.-D. Wang, Y.-F. Xu, H.-Y. Chen, D.-B. Kuang, and C.-Y. Su, *ACS Energy Lett.* **3**, 2613 (2018), <https://doi.org/10.1021/acsenerylett.8b01770>.
- [20] M. C. Folgueras, J. Jin, M. Gao, L. N. Quan, J. A. Steele, S. Srivastava, M. B. Ross, R. Zhang, F. Seeler, K. Schierle-Arndt, M. Asta, and P. Yang, *J. Phys. Chem. C* **125**, 25126 (2021), <https://doi.org/10.1021/acs.jpcc.1c08332>.
- [21] H. Wan, F. Jia, F. Dinic, M. Imran, B. Rehl, Y. Liu, W. Paritmongkol, P. Xia, Y.-K. Wang, Y. Liu, S. Wang, Q. Lyu, G. F. Cotella, P. Chun, O. Voznyy, S. Hoogland, and E. H. Sargent, *Chem. Mater.* **35**, 948 (2023), <https://doi.org/10.1021/acs.chemmater.2c02673>.
- [22] B. Glockzin, M. S. Oakley, A. Karmakar, A. Pominov, A. A. Mitchell, X. Ma, M. Klobukowski, and V. K. Michaelis, *J. Phys. Chem. C* **127**, 7284 (2023), <https://doi.org/10.1021/acs.jpcc.2c08073>.
- [23] X. Qiu, B. Cao, S. Yuan, X. Chen, Z. Qiu, Y. Jiang, Q. Ye, H. Wang, H. Zeng, J. Liu, and M. Kanatzidis, *Sol. Energy Mater. Sol. Cells* **159**, 227 (2017), publisher Copyright: © 2016 Elsevier B.V.
- [24] M. Rohlffing and S. G. Louie, *Phys. Rev. Lett.* **81**, 2312 (1998).
- [25] J. Heyd, G. E. Scuseria, and M. Ernzerhof, *J. Chem. Phys.* **118**, 8207 (2003), [https://pubs.aip.org/aip/jcp/article-pdf/118/18/8207/10847843/8207\\_1\\_online.pdf](https://pubs.aip.org/aip/jcp/article-pdf/118/18/8207/10847843/8207_1_online.pdf).
- [26] L. Hedin, *Phys. Rev.* **139**, A796 (1965).
- [27] G. Kresse and J. Furthmüller, *Phys. Rev. B* **54**, 11169 (1996).
- [28] G. Kresse and J. Furthmüller, *Comput. Mater. Sci.* **6**, 15 (1996).
- [29] J. J. Mortensen, L. B. Hansen, and K. W. Jacobsen, *Phys. Rev. B* **71**, 035109 (2005).
- [30] J. P. Perdew, K. Burke, and M. Ernzerhof, *Phys. Rev. Lett.* **77**, 3865 (1996).
- [31] L. Hedin, *Phys. Rev.* **139**, A796 (1965).
- [32] M. S. Hybertsen and S. G. Louie, *Phys. Rev. Lett.* **55**, 1418 (1985).
- [33] S. Albrecht, L. Reining, R. Del Sole, and G. Onida, *Phys. Rev. Lett.* **80**, 4510 (1998).
- [34] M. Rohlffing and S. G. Louie, *Phys. Rev. Lett.* **81**, 2312 (1998).
- [35] M. Gajdoš, K. Hummer, G. Kresse, J. Furthmüller, and F. Bechstedt, *Phys. Rev. B* **73**, 045112 (2006).
- [36] G. Thiele, C. Mrozek, D. Kämmerer, and K. Wittmann, *Z. Naturforsch. 38b* **38**, 905 (1983).
- [37] D. I. Torres, J. D. Freire, and R. S. Katiyar, *Phys. Rev. B* **56**, 7763 (1997).
- [38] J. Ketelaar, A. Rietdijk, and C. Van Staveren, *Recl. Trav. Chim. Pays-Bas* **56**, 907 (1937).
- [39] W. Werker, *Recl. Trav. Chim. Pays-Bas* **58**, 257 (1939).
- [40] G. Engel, *Z. Kristallogr Cryst. Mater.* **90**, 341 (1935).
- [41] Q. Mahmood, M. Hassan, T. H. Flemban, B. Ul Haq, S. AlFaify, N. A. Kattan, and A. Laref, *J. Phys. Chem. Solids* **148**, 109665 (2021).
- [42] S. Suzuki and M. Tsuyama, *Opt. Mater.* **119**, 111323 (2021).
- [43] S. de Gironcoli, *Phys. Rev. B* **51**, 6773 (1995).
- [44] F. Mouhat and F. m. c.-X. Coudert, *Phys. Rev. B* **90**, 224104 (2014).
- [45] V. Wang, N. Xu, J.-C. Liu, G. Tang, and W.-T. Geng, *Comput. Phys. Commun.* **267**, 108033 (2021).
- [46] Z.-j. Wu, E.-j. Zhao, H.-p. Xiang, X.-f. Hao, X.-j. Liu, and J. Meng, *Phys. Rev. B* **76**, 054115 (2007).
- [47] R. Hill, *Proc. Phys. Soc. A* **65**, 349 (1952).
- [48] S. Pugh, S. Pugh **45**, 823 (1954), <https://doi.org/10.1080/14786440808520496>.
- [49] B. Huang, Y.-H. Duan, W.-C. Hu, Y. Sun, and S. Chen, *Ceram. Int.* **41**, 6831 (2015).
- [50] J.-M. Zhang, Y. Zhang, K.-W. Xu, and V. Ji, *J. Phys. Chem. Solids* **68**, 503 (2007).
- [51] S. I. Ranganathan and M. Ostojica-Starzewski, *Phys. Rev. Lett.* **101**, 055504 (2008).
- [52] M.-G. Ju, J. Dai, L. Ma, and X. C. Zeng, *Adv. Energy Mater.* **7**, 1700216 (2017), <https://onlinelibrary.wiley.com/doi/pdf/10.1002/aenm.201700216>.
- [53] Q. Li, L. Zhou, Y. Ge, Y. Ren, J. Zhao, W. Wan, K. Zhang, and Y. Liu, arXiv preprint arXiv:1908.02187 (2019), arXiv:1908.02187 [physics.app-ph].
- [54] T. I. Al-Muhimeed, A. Shafique, A. A. AlObaid, M. Morsi, G. Nazir, M. m. AL-Anazy, and Q. Mahmood, *Int. J. Energy Res.* **45**, 19645 (2021), <https://onlinelibrary.wiley.com/doi/pdf/10.1002/er.7022>.
- [55] S. Chadli, A. Bekhti Siad, M. Baira, M. Siad, A. Allouche, and A. Reguig, *Solid State Commun.* **342**, 114633 (2022).
- [56] S. A. Qamar, T.-W. Lin, Y.-T. Tsai, and C. C. Lin, *ACS Appl. Nano Mater.* **5**, 7580 (2022), <https://doi.org/10.1021/acsanm.2c01647>.
- [57] A. E. Maughan, A. M. Ganose, M. A. Almaker, D. O. Scanlon, and J. R. Neilson, *Chem. Mater.* **30**, 3909 (2018), <https://doi.org/10.1021/acs.chemmater.8b01549>.
- [58] D. Hemidi, T. Seddik, T. Benmessabih, M. Batouche, W. Ouerghui, H. B. Abdallah, G. Surucu, and S. Ahmad, *Appl. Phys. A: Mater. Sci. Process.* **129**, 762 (2023).
- [59] M. Kumar, A. Singh, D. Gill, and S. Bhattacharya, *J. Phys. Chem. Lett.* **12**, 5301 (2021), PMID: 34061540, <https://doi.org/10.1021/acs.jpcclett.1c01034>.
- [60] M. Bokdam, T. Sander, A. Stroppa, S. Picozzi, D. D. Sarma, C. Franchini, and G. Kresse, *Sci. Rep.* **6**, 28618 (2016).
- [61] X. Wang, W. Meng, and Y. Yan, *J. Appl. Phys.* **122**, 10.1063/1.4991913 (2017), [https://pubs.aip.org/aip/jap/article-pdf/doi/10.1063/1.4991913/15201223/085104\\_1\\_online.pdf](https://pubs.aip.org/aip/jap/article-pdf/doi/10.1063/1.4991913/15201223/085104_1_online.pdf).
- [62] F. Ferreira, A. J. Chaves, N. M. R. Peres, and R. M. Ribeiro, *J. Opt. Soc. Am. B* **36**, 674 (2019).
- [63] M. R. Filip, J. B. Haber, and J. B. Neaton, *Phys. Rev. Lett.* **127**, 067401 (2021).
- [64] R. W. Hellwarth and I. Biaggio, *Phys. Rev. B* **60**, 299 (1999).

- [65] J. M. Frost, *Phys. Rev. B* **96**, 195202 (2017).
- [66] C. Franchini, M. Reticcioli, M. Setvin, and U. Diebold, *Nat. Rev. Mater.* **6**, 560 (2021).
- [67] R. P. Feynman, *Phys. Rev.* **97**, 660 (1955).
- [68] P. Bhumla, M. Jain, S. Sheoran, and S. Bhattacharya, *J. Phys. Chem. Lett.* **13**, 11655 (2022), pMID: 36503226, <https://doi.org/10.1021/acs.jpcclett.2c02852>.